Surface Permanent Magnet Synchronous Machines: High Speed Design and Limits

Gianvito Gallicchio, Mauro Di Nardo, *Member, IEEE,* Marco Palmieri, *Member, IEEE,* Mohammad Reza Ilkhani, Michele Degano, *Senior Member, IEEE,* Chris Gerada, *Senior Member, IEEE,* and Francesco Cupertino, *Senior Member, IEEE*

***Abstract*—Surface permanent magnet synchronous machines are one of the most widely adopted machine topologies in high-speed applications where efficiency and power factor cannot be compromised. Although the design of such machine type has been extensively investigated in both industry and academia, this work aims at addressing its limitations when applied in high-speed applications. First, this paper proposes an accurate design methodology for continuous-duty high-speed surface-mounted permanent magnets synchronous machines, capable of accounting for the rise of the speed-dependent losses and structural needs with a limited impact on the computational burden. The outlined approach can be used to speed-up the initial design stage as it allows to reduce the number of solutions to evaluate before commencing the refinement stages required before the definition of the final design. Indeed, the introduced design approach is used to systematically assess the maximum power capability as function of the maximum speed and the airgap thickness for a given outer envelope and cooling system. The influence of the high-speed limiting factors is deeply investigated also considering their effects on the machine geometries providing the highest torque. The selection of the final design is discussed and justified. Experimental results of the 4.2kW-80kprm prototype validate the design methodology.**

***Index Terms*—Analytical design, finite element analysis, high speed, permanent magnet motor, power density, sleeve, structural rotor design, synchronous motor.**

I. Introduction

Permanent Magnets Synchronous Machines (PMSMs) constitute a widespread solution for those applications requiring high torque density, efficiency and power factor [1]–[3]. In the last decade the research has been oriented towards the development of electrical machines featuring enhanced power densities in order to meet the increasing needs of the transportation and industrial electrification processes [4], [5]. For a given target power, the adoption of high rotational speed implies a lower electromagnetic torque, with a consequent reductions of both size and weight. Moreover, it can lead to better efficiency, higher reliability and easier maintenance because it allows direct-drive arrangements, eliminating the need of mechanical gear-boxes. Beside those benefits, the design of high speed machines poses significant challenges in terms of material selection, loss minimization and thermal management [6], [7]. Core losses increase with the speed together with centrifugal forces: therefore a multi-physics approach is required to address the strong interconnection between electromagnetic, thermal and mechanical design aspects [8]. PM materials feature high compressive strength and low tensile strength, therefore they cannot withstand the centrifugal force generated by high rotational speed (when using dovetail inserts). In order to guarantee the structural integrity, the PMs are usually encapsulated using retaining sleeves which pre-stress the material to compensate the centrifugal force at high speed operation [9]. This leads to two major drawbacks: firstly, the magnetic airgap becomes wider, with a consequent reduction of the average torque; secondly, depending on its composition, the sleeve can increase the total losses or can worsen the heat extraction from the rotor structure. In fact, sleeves can be made of non magnetic metallic materials (e.g. stainless steel, titanium alloy, inconel) or composite ones (i.e. carbon fiber reinforced plastic). The former facilitate the heat removal from the rotor thanks to their superior thermal conductivity, but are prone to higher eddy current losses due to their good electrical conductivity; the latter show an enhanced weight to strength ratio but present opposite features in terms of thermal and electrical conductivity with respect to metallic sleeves [9], [10].

The other high-speed challenge is represented by the thermal management due to the increment of all loss components. Indeed, it affects the choices of the soft magnetic material (silicon-steel or cobalt-iron alloys), the wire type (random or litz wire) and the cooling system.

When comparing different machines, either different machine types or different designs of the same topology, the exercise can be performed considering either a constant current density or a constant stator loss scenario. In the first case, the cooling system needs to be designed according to the considered machine while in the latter it can remain invariant, making fairer the machine comparison [11].

In literature, several works have addressed the design of high speed PMSMs. A typical approach starts with a pure electromagnetic design, which neglects the influence of the sleeve, aimed at obtaining the main machine parameters [12], [13]; then, a mechanical parametric study [10], [14], [15] is performed to evaluate the rotor stress, size the sleeve and refine the final design. Other approaches consider the electromagnetic and structural designs within the same workflow, either using simplified analytical models [16], [17] or

G. Gallicchio and F. Cupertino are with the Department of Electrical Engineering and Information Technology, Politecnico di Bari, Bari, 70126 Italy e-mail: gianvito.gallicchio@poliba.it.

M. Di Nardo, M. Ilkhani, M. Degano and C. Gerada are with the Power Electronics, Machines and Control Group, University of Nottingham, Nottingham, NG7 2GT, UK.

M. Palmieri is with the School of Engineering, Università degli studi della Basilicata, Potenza, 85100, Italy.

more sophisticated approaches based on finite element analysis (FEA) [18]–[20]. It is worth to highlight that most of these approaches, analytical or FE-based, either start with a given stator design or do not consider the sleeve sizing within the electromagnetic design routine or do not keep the total losses constant when comparing different geometries.

Therefore, the aim of this paper is to propose a comprehensive design procedure able to consider the main aspects involved during the design of high speed PMSMs when a metallic sleeve is adopted. Starting from few assumptions, a couple of independent geometric variables are identified as design inputs and the main performance indexes are evaluated as their function through analytical relations refined with few FE simulations. In particular, the design routine adopted in [11], [21], [22] for synchronous reluctance machines is here modified to correctly account for the surface mounted PM rotor.

The proposed design approach allows to compare different machine geometries and help the designer to first infer the relations between thermal, structural and electromagnetic needs and select the machine which allows the maximization of a predefined design target, thus leading to the second-stage design process which is mainly a refinement stage.
According to the above consideration, the method is then used to asses the maximum power capability of PMSMs for given stator losses as the maximum design speed increases. The effects of the performance limiting factors on both optimal torque and related machine geometry are assessed through the proposed optimal design flowchart. In addition, the influence of the airgap thickness is also investigated in terms of trade-off between torque and rotor losses, as well as optimal geometries.

The paper is organized as follows: section II describes the analytical procedure while section III presents its FE validation along with a FE-adjustment routine capable of taking into account all the analytical modeling inaccuracies. The procedure is then used in section IV to investigate the machine performance for several values of speed and airgap thickness, while a discussion about the optimal designs and the reasons behind the final choice are reported in section V. Finally, the methodology is validated in section VI where experimental results on a 4.2kW-80krpm machine are provided.

II. Analytical design procedure

Both performance and geometry of a surface-mounted PMSM can be defined by two independent design variables: the split ratio sr (the ratio between the airgap radius r_r, i.e. the internal stator radius minus half of the airgap thickness, and the external radius r_s) and the magnetic ratio mr (the ratio between the first harmonic of the airgap flux density B_g and the peak value of the flux density in the stator yoke B_{fe}):

$$sr = \frac{r_r}{r_s} \tag{1}$$

$$mr = \frac{B_g}{B_{fe}} \tag{2}$$

The following assumptions and constraints are also considered:

- the external dimensions (i.e external radius r_s and active axial length l_{fe}) are imposed;

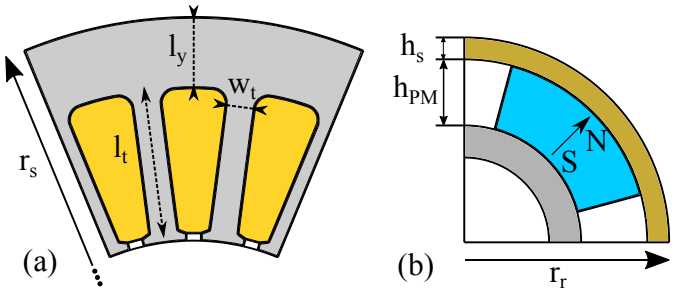

Fig. 1: Stator (a) and rotor (b) parametrization.

- the flux density B_{fe} within the stator yoke and teeth is preliminary fixed (generally close to the knee point of the $B-H$ curve of the stator core material);
- the cooling system capability is chosen in terms of total losses that can be extracted via the outer stator surface.

It is well known that the torque produced by an isotropic synchronous PM machine can be expressed as in (3):

$$T = \frac{3}{2} \cdot p \cdot \lambda_{PM} \cdot i_q \tag{3}$$

where p is the number of pole pairs, λ_{PM} is the no-load PM flux linkage and i_q is the q-axis stator current component. In the following, each geometric parameter, depicted in Fig. 1, as well as the stator current, flux linkage and so the torque are expressed as function of both sr and mr.

A. Stator design

The stator main paramaters are the tooth width w_t, the yoke thickness l_y and the tooth length l_t. The first one can be determined imposing the flux flowing the tooth to be equal to the integral of the airgap flux density over the slot pitch, whereas the second can be calculated imposing the flux within the stator yoke to be equal to half of the flux per pole, thus obtaining the following relationships [13]:

$$w_t = \frac{2 \cdot \pi \cdot r_s}{6 \cdot p \cdot q} \cdot \frac{B_{g-max}}{B_g} \cdot sr \cdot mr \cdot k_t \tag{4}$$

$$l_y = \frac{\alpha_{PM} \cdot \pi \cdot r_s}{2 \cdot p} \cdot \frac{B_{g-max}}{B_g} \cdot sr \cdot mr \tag{5}$$

where q is the number of slots per pole per phase, B_{g-max} is the peak value of the airgap flux density, α_{PM} is the PM angular span, and k_t is the tooth factor which has been set to 0.9 (i.e. the imposed flux density for the teeth is 10% higher with respect to the yoke). The last main geometrical parameter identifying the tooth length follows by geometrical considerations:

$$l_t = r_s - r_r - l_y - l_{ts} \tag{6}$$

where l_{ts} is the tooth shoe height that, together with the slot opening, complete the description of the stator geometry. All these secondary parameters have been preliminary defined. In particular, in this work, a trapezoidal slot configuration featuring a slot opening equal to 0.25 (in p.u. of the slot pitch) and a ratio between l_{ts} and w_t equal to 0.25 have been considered for all machine designs.

B. Maximum current calculation

The q-axis current can be considered equal to the maximum available current I_{max} if only the operation in the maximum torque per ampere condition is envisaged. As the cooling capacity is preliminary chosen (through the factor k_{cool} equal to the ratio between the total losses and the external surface of the stator), the maximum current can be calculated imposing the sum of Joule and iron losses P_{fe} to be equal to the maximum capability of the cooling system:

$$I_{max} = \frac{1}{3N_s}\sqrt{\frac{k_{fill}A_{slots}}{2\rho_{cu}(l_{fe}+l_{ew})}(2\pi r_s l_{fe} k_{cool} - P_{fe})} \quad (7)$$

where k_{fill} is the imposed filling factor, ρ_{cu} is the copper resistivity and N_s is the number of turns in series per phase. The slots area A_{slots} and the end-winding length l_{ew} can be expressed as function of the design variables as in (8) and (9) respectively:

$$A_{slots} = \frac{6\cdot q\cdot p\cdot l_t}{2}\cdot\left[\frac{2\pi(sr\cdot R_s+g+l_{ts})}{6\cdot q\cdot p}+ \right. \\ \left. +\frac{2\pi(sr\cdot R_s+g+l_t)}{6\cdot q\cdot p} - 2w_t\right] \quad (8)$$

$$l_{ew} = 2l_t + \left(sr\cdot r_s + \frac{l_t}{2}\right)\frac{\pi}{p} \quad (9)$$

The stator iron losses affect the maximum current of the machine under consideration and are initially estimated using the Steinmetz formulation [23]:

$$P_{fe} = k_{fe}M_{fe}[k_h f^{\alpha} B_{fe}^{\beta} + k_e(fB_{fe})^2] \quad (10)$$

where k_{fe} is a correction factor (usually between 1-2), M_{fe} is the stator iron mass, f is the electrical frequency, k_h, k_e, α and β are the material coefficients.

It is worth to underline that the selected current calculation criterion allows to keep constant the total stator iron losses over the $sr-mr$ plane. Thus, sleeve and PM eddy current losses are not considered for the current calculation. The friction and windage losses have also not been considered during the current calculation as they constitute a minor part of the overall losses.

C. Rotor design: magnetic equivalent circuit

Neglecting the tangential component of the airgap flux density, the PM height can be calculated by solving the magnetic circuit reported in Fig. 2 preliminary choosing the angular span of the PM over the pole pitch. Indeed, the peak value of the total magnetic voltage has to be equal to the current linkage $H_c\cdot h_{PM}$, as in (11):

$$2\cdot U_g + 2\cdot U_{st} + U_{sy} + U_{ry} + 2\cdot U_{PM} = 2\cdot H_c\cdot h_{PM} \quad (11)$$

where U_g, U_{sy}, U_{ry}, U_{st} and U_{PM} are the airgap, stator yoke, rotor yoke, stator teeth and PM magnetic voltage drops. It is worth to notice that U_{PM} is also function of the PM height:

$$U_{PM} = \frac{H_c}{B_r}\cdot B_{g-max}\cdot h_{PM} \quad (12)$$

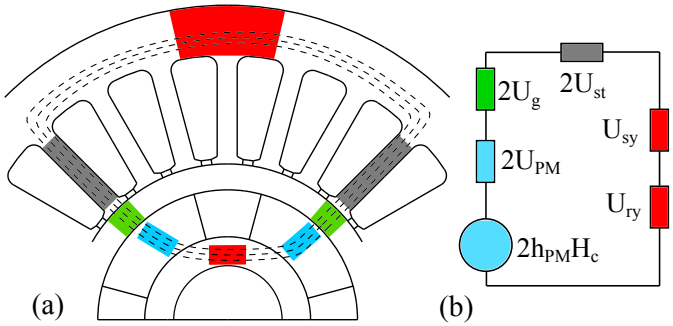

Fig. 2: a) Flux path due to PMs; b) magnetic equivalent circuit.

where H_c and B_r are the coercive field and residual flux density of the PM. By combining (11) and (12), the PM height can be finally computed as in (13):

$$h_{PM} = \frac{2\cdot U_g + 2\cdot U_{st} + U_{sy} + U_{ry}}{2\cdot Hc\cdot\left(1-\frac{B_{g-max}}{B_r}\right)} \quad (13)$$

The stator yoke, rotor yoke and stator teeth magnetic voltage drops do not depend on the sleeve thickness since the magnetic load B_{fe} is imposed. Conversely, as reported in (14), U_g is affected by the sleeve dimension, since it is a function of the equivalent magnetic airgap (which is the sum of the mechanical one g and the sleeve thickness h_s):

$$U_g = \frac{B_{g-max}}{\mu_0}\cdot(g+h_s) \quad (14)$$

D. Sleeve computation

The retaining sleeve role is twofold: secure the PMs at high speed and exert the proper pressure on the magnets and consequently on the shaft in order to transfer the machine maximum torque. These functionalities need to be guaranteed in any thermal operating condition. Super-alloys are usually used when considering metallic sleeves as they feature high mechanical strength and robust behaviour at high temperatures. From a conceptual point of view, sleeve, magnets and shaft can be all considered as cylinders that interact between each other through the pressure at their boundaries. Several analytical approaches have been proposed in literature to analyse the stress in concentric cylinders [24], [25]. Among these formulations, the plane stress in thick cylinder, also known as Lame formula, is a good approach as not only covers both the mechanical and thermal effects but also has an exact solution for this particular application. In order to derive the equilibrium equations, the 2D cross-sections of the shaft, magnets, and sleeve are considered as three cylinders. The static equilibrium equation for the isotropic thick cylinder under centrifugal body force and temperature gradient can be written as follows:

$$\frac{E_l}{1-\nu_l^2}\left(\frac{\mathrm{d}^2u_{r_l}}{\mathrm{d}r^2}+\frac{1}{r}\frac{\mathrm{d}u_{r_l}}{\mathrm{d}r}-\frac{u_{r_l}}{r^2}-\beta_l(1+\nu_l)\frac{\mathrm{d}\Delta T_l}{\mathrm{d}r}\right)+ \\ +\rho_l r\Omega^2 = 0 \quad (15)$$

where u_r is the displacement as a function of radial position, r is the radial coordinate, E is the module of elasticity, ν

is the Poisson ratio, β is the coefficient of thermal expansion, ΔT is the temperature variation function in the radial direction, ρ is the density, Ω is the rotational speed, while the subscript $l = sh, pm, s$ stands for shaft, magnet and sleeve, respectively. These three ordinary differential equations have a homogeneous and a particular solution:

$$u_{r_l} = C_{1_l} r + \frac{C_{2_l}}{r} + \beta_l(1+\nu_l)\frac{1}{r}\int_{r_{in}}^{r} \Delta T_l r dr + \\ - \frac{\rho_l \Omega^2 (1-\nu_l^2) r^3}{8E_l} \tag{16}$$

where u_r is the displacement as a function of radial position, and C_1 and C_2 are the unknown constants that are determined by imposing the boundary conditions. As the displacement functions are three, one for the shaft, magnet and sleeve, there are six unknown constants that need to be determined. Based on the interaction at the boundaries of these parts, the following boundary conditions have been applied to find these six unknown coefficients:

$$\begin{aligned} \sigma_{r_{sh}} &\neq \infty @ (r=0), \\ \sigma_{r_{sh}} &= \sigma_{r_{pm}} @ (r = r_{sh}), \\ u_{r_{pm}} - u_{r_{sh}} &= \delta_{sh-pm} @ (r = r_{sh}), \\ \sigma_{r_{pm}} &= \sigma_{r_s} @ (r = r_{pm}), \\ u_{r_s} - u_{r_{pm}} &= \delta_{pm-s} @ (r = r_{pm}), \\ \sigma_{r_s} &= 0 @ (r = r_s), \end{aligned} \tag{17}$$

where σ_{r_l} with $l = sh, pm, s$ is radial stress in the indicated layers, δ_{sh-pm} is the difference between the bore of magnets and outer diameter of shaft, and δ_{pm-s} is the difference between the sleeve's bore and outer diameter of magnet before assembly that when assembled show themselves as interference and create stress. Four of the above equations impose conditions on the radial stress while two set the interference needed at the interfaces between shaft-magnet and magnet-sleeve. Since the radial stress is required to impose the boundary conditions, displacement-strain and stress-strain relations (for isotropic material) need to be expressed:

$$\epsilon_{r_l} = \frac{\mathrm{d}u_l}{\mathrm{d}r}, \epsilon_{\theta_l} = \frac{u_{r_l}}{r}, \tag{18}$$

$$\begin{aligned} \epsilon_{r_l} &= \frac{1}{E_l}(\sigma_{r_l} - \nu\sigma_{\theta_l}) + \beta_l \Delta T_l, \\ \epsilon_{\theta_l} &= \frac{1}{E_l}(\sigma_{\theta_l} - \nu\sigma_{r_l}) + \beta_l \Delta T_l, \end{aligned} \tag{19}$$

where ϵ_r and ϵ_θ are strain in radial and circumferential directions, respectively. By replacing the displacement expression (16) into the strain relations (18) and (19), the stress expression in radial direction can be obtained. By setting geometrical constraints, operating speed, material properties and required interference values, a set of six algebraic linear equations is obtained whose solution provides the six unknown constants.

The previous system of equations allows obtaining the radial and circumferential displacements and stresses in all components as function of the radius for a given rotor structure (defined by the external rotor radius r_r, sleeve and PM thicknesses h_s, h_{pm}, and interferences $\delta_{sh-pm}, \delta_{pm-s}$). In order to verify if the geometry under consideration represents a functional and a reliable design, the following conditions need to be met:

1) the compressive radial stress between shaft and magnet should be more than the value required to transmit the maximum torque;
2) the interference between magnets and sleeve should be less than $0.2\mathrm{mm}$ as a higher value would cause practical problems during the shrink fitting of the sleeve;
3) the maximum Von Mises stress in the PM should not exceed its ultimate strength and the radial stress should be compressive rather than tensional as PM materials feature low tensile strength;
4) the maximum Von Mises stress σ_{sl}^{VM} in the sleeve should be less than the material yield strength to avoid any plastic deformation and subsequent failure.

Fig. 3 shows the maximum Von Mises stress in the sleeve for a wide range of rotor geometries featuring a given outer radius and several magnet and sleeve thicknesses when the conditions 1)-3) are satisfied. In this case study, the maximum Von Mises stress in the sleeve has been set to 750 MPa and the black markers identify the maximum permanent magnet dimensions (h_{PM-max}) that a given sleeve thickness can support without exceeding any limits. Repeating such parametric study for several rotor outer radii, it is possible to derive the maximum magnet thickness as function of the sleeve dimensions for several rotor outer radii as shown in Fig. 4.

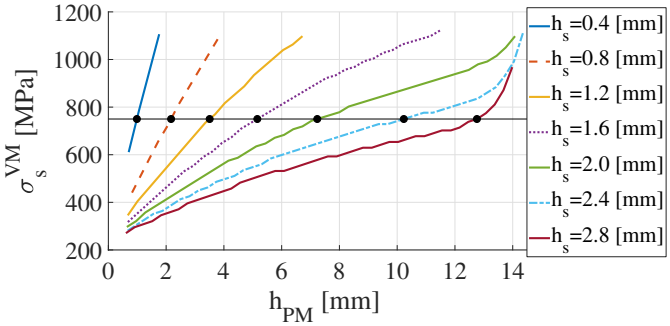

Fig. 3: Maximum Von Mises stress in the sleeve as function of magnet and sleeve thicknesses at 80 krpm for a given outer rotor radius r_r=18 mm.

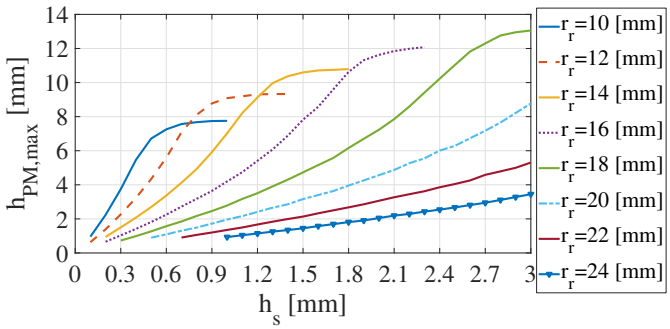

Fig. 4: Maximum PM thickness as function of the sleeve thickness for different outer rotor radii at 80 krpm.

E. Iterative calculation of PM and sleeve thicknesses

Analysing eq. (13) and (14) follows that the sleeve and the PM thicknesses can not be independently calculated as the sleeve presence affects the magnetic performance and the PM dimensions influence the sleeve dimensions. As a consequence, an iterative procedure is required to identify these two parameters. In particular, first the h_{PM} is calculated by (13) considering $h_s = 0$ in (14). Then, the sleeve calculation procedure of section II-D is applied so to determine the value of h_s required to sustain the above computed h_{PM} for the considered rotor radius and maximum speed. The obtained h_s is then used to update the airgap magnetic voltage drop in (14) leading to the computation of a new h_{PM} still using (13). This iterative procedure ends when the absolute error between the values of h_s for two consecutive iterations becomes lower than a predefined threshold.

III. Design approach validation and adjustment

The proposed analytical procedure permits an accurate prediction of the electromagnetic performance for a wide range of $sr - mr$ combinations, thus allowing to compare different geometries for a given set of design assumptions with a reduced computational burden. This analytical procedure has been applied to design and analyze machines considering the constraints and the assumptions reported in Table I and a maximum speed equal to 40 krpm. In this section, first the quality of the electromagnetic performance estimation is assessed against the full FEAs, then a FE adjustment procedure is proposed to alleviate the pitfalls of the analytical formulations. Lastly, the thermal performance of a large set of machines are investigated in order to assess the validity of the constant stator loss design criteria.

TABLE I: Design constraints and assumptions

Parameter	Value	Units
Outer stator radius	30	mm
Stack length	30	mm
Pole pairs	2	/
N° of stator slots	24	/
PM material	Recoma 28	/
Stator material	10JNHF600	/
Sleeve material	Inconel 718	/
Iron flux density	1.4	T
Cooling capability	23	kW/m^2

A. Electromagnetic performance validation

Fig. 5c shows the torque contours in the $sr - mr$ design plane evaluated with the described analytical model and those obtained by FEA. The visible discrepancy is mainly due to the inaccuracy of the analytical model in predicting the iron losses and the PM flux linkage as shown in Fig. 5a, b.

The iron losses mismatches can be ascribed to:

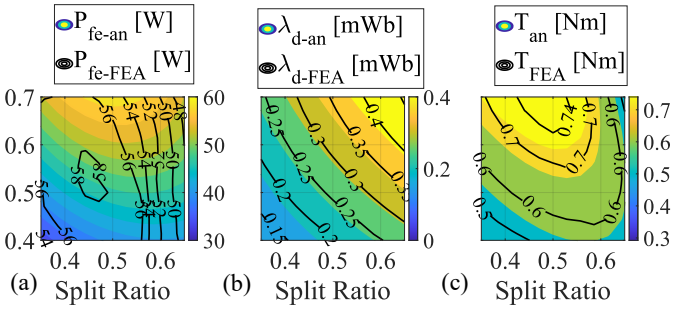

Fig. 5: Comparison between analytical results and FE ones: (a) iron losses; (b) d-axis flux and (c) electromagnetic torque.

- the peak value of the flux density in yoke and teeth in load condition (B_{fe}) which is not constant in the $sr-mr$ plane;
- the influence of the harmonic iron losses.

The B_{fe} imposed during the design stage refers to the no-load condition (i.e. $i_q = 0$), since the magnetic equivalent circuit and the calculation of the stator tooth and yokes is performed only considering the PM contribution (a common procedure for PMSMs [13]). Fig. 6 reports the FE-computed peak values of flux density within yoke (a,c) and teeth (b,d) at no-load (a,b) and load conditions (c,d) over the $sr-mr$ plane for a 40 krpm case. It is worth to notice that the FE no-load B_{fe} is almost constant over the $sr-mr$ plane as imposed during the design process for both the yoke and teeth. Differently, in the load scenario the effects of the stator magnetomotive force due to the i_q contribution lead to a non-uniform distribution of the flux density. This non-uniform distribution of B_{fe} is the main reason behind the qualitative iron losses mismatches shown in Fig. 5a. Indeed, the analytical iron losses shown in Fig. 7a clearly match those computed using the peak value of the no-load flux density of Fig. 7b from a qualitative point of view.

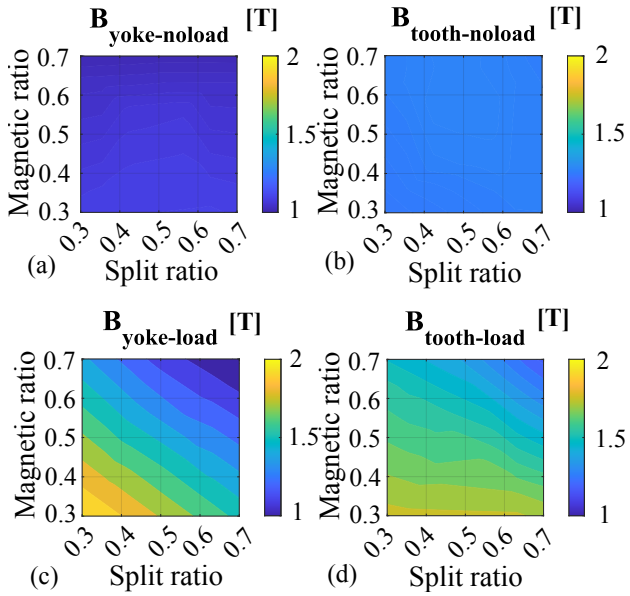

Fig. 6: No load (a,b) and load (c,d) peak value of the flux density within stator yoke (a,c) and stator tooth (b,d) in the $sr - mr$ plane

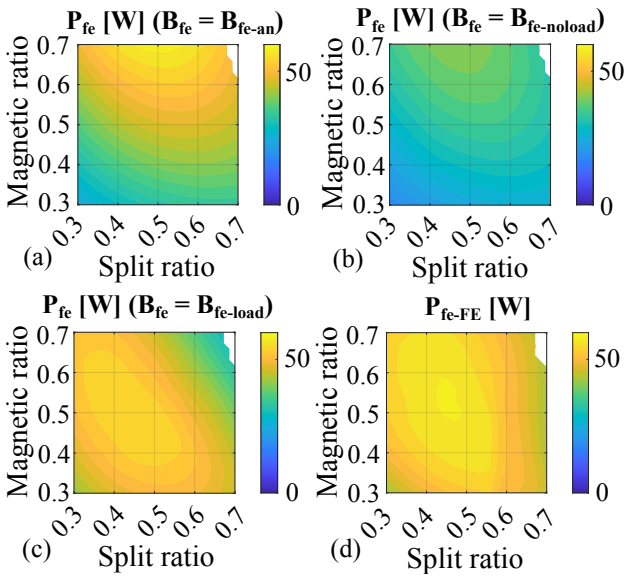

Fig. 7: Analytical stator iron losses (a); stator iron losses calculated using the peak value of FE-computed B_{fe} at no-load (b) and load (c) conditions; actual FE iron losses (d).

On the contrary, when the peak value of the FE-computed B_{fe} is used in the Steinmetz's equation, the stator iron losses contours clearly have a different shape (Fig. 7c) which in turn resembles the one of the actual FE-computed iron losses (Fig. 7d). It can be concluded that the iron loss discrepancy can be mainly ascribed to the non-uniform distribution in the $sr-mr$ plane of B_{fe} within yoke and teeth; the residual mismatches are due to the minor cause (i.e. the harmonic iron losses).

B. FE adjustment

With the aim of tackling the above issues, the FE-adjustment procedure reported in [11] for synchronous reluctance machines is here extended to include the PMSM design scenario. In particular, the machines at the corners of the design plane $sr-mr$ are FE-simulated in order to accurately evaluate their iron losses and so the ratio between the FE and analytical losses. Such iron loss correction factor is then extended to the overall design plane using a linear interpolation. The analytical design is then re-carried out by updating the stator current (eq. (7)) until the iron losses error becomes negligible.

Once the iron losses of the corner machines and so their maximum currents have been identified, the correction factors for the d- and q-axis fluxes are FE calculated. The extension of these correction factors to the overall design plane leads to the adjustment of the magnetic model. The comparison between the adjusted torques and the FE ones shown in Fig. 8c is excellent as expected and it is due to a more reliable estimation of iron losses and d-axis flux reported in Fig. 8a and b respectively. It is worth to underline that the corrected torque average error is about 2% highlighting the accuracy of the proposed approach. In addition, the maximum error is always located away from the maximum torque region, which is the area of final interest.

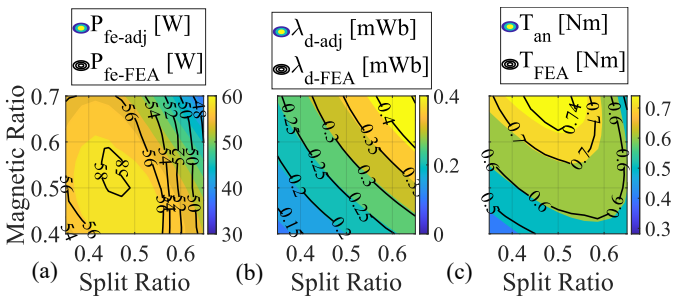

Fig. 8: Comparison between analytical adjusted results and FE ones: (a) iron losses; (b) d-axis flux and (c) electromagnetic torque.

C. Thermal performance validation

The constant stator losses design criteria, used throughout the proposed comparative design exercise, is meant to lead to thermal performance that do not substantially differ from one machine to another. This statement is based on the strong assumption that the temperature distribution within the machine mainly depend from the overall losses while their distribution (between iron and copper) plays a minor role. Fig. 9a reports the winding temperature in the $sr-mr$ plane considering a design speed of 40krpm and an airgap thickness of 1 mm. The thermal performance at steady-state conditions have been estimated using the commercial software [26] adopting a spiral water jacket as cooling system whose details will be reported in the experimental section. All the losses contributions including the rotor ones (PM, sleeve, rotor core and mechanical ones) are included within the thermal analysis. The winding temperature is almost constant within the design plane and the difference between the highest and lower temperature is around 15°C (when excluding extreme machine designs at the border of the design plane). The winding temperature contour clearly resembles the constant loci of the ratio between iron and copper stator losses shown in Fig. 9b. As expected, the winding temperature is lower in the regions of the design plane characterized by higher iron losses and lower copper losses.

It can be concluded that the constant stator losses design criteria constitutes a valid approach as it leads to machine designs with comparable stator thermal performance without directly evaluating the latter within the design workflow.

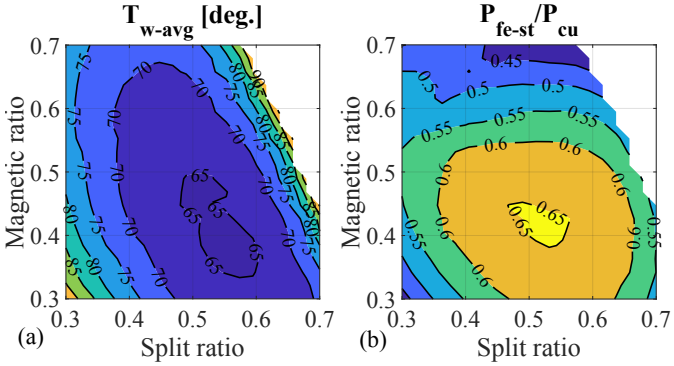

Fig. 9: (a) Estimated winding average temperature and (b) ratio between iron and copper stator losses in the sr-mr plane at 40krpm.

IV. High speed designs

The proposed design procedure is hereafter used to investigate the influence of the maximum speed and the airgap thickness on the machine performance. The parameters which do not change within all the analysis are those listed in Table I; the remaining ones are calculated for each $sr - mr$ combination according to the procedure described in section II. Fig. 10 reports the constant torque loci in the $sr - mr$ plane for different rotational speeds (40, 60 and 80 kprm) and airgap thickness (0.5, 1, 1.5 and 2 mm), along with a marker highlighting the maximum torque design (hereafter called optimal design). As expected, the torque is negatively affected by the speed and airgap increases. This is mainly due to the increment of the iron losses (affecting the stator current) and to the sleeve thickness which widenes the equivalent magnetic airgap, leading to a higher flux leakage for a given combination of sr and mr. As the speed increases, for a given airgap thickness, the optimal design moves towards lower magnetic ratios while the split ratio remains almost constant; the same trend is observed moving from small to large airgap, for a given maximum speed. In the following subsections, the reasons behind such behaviours are investigated.

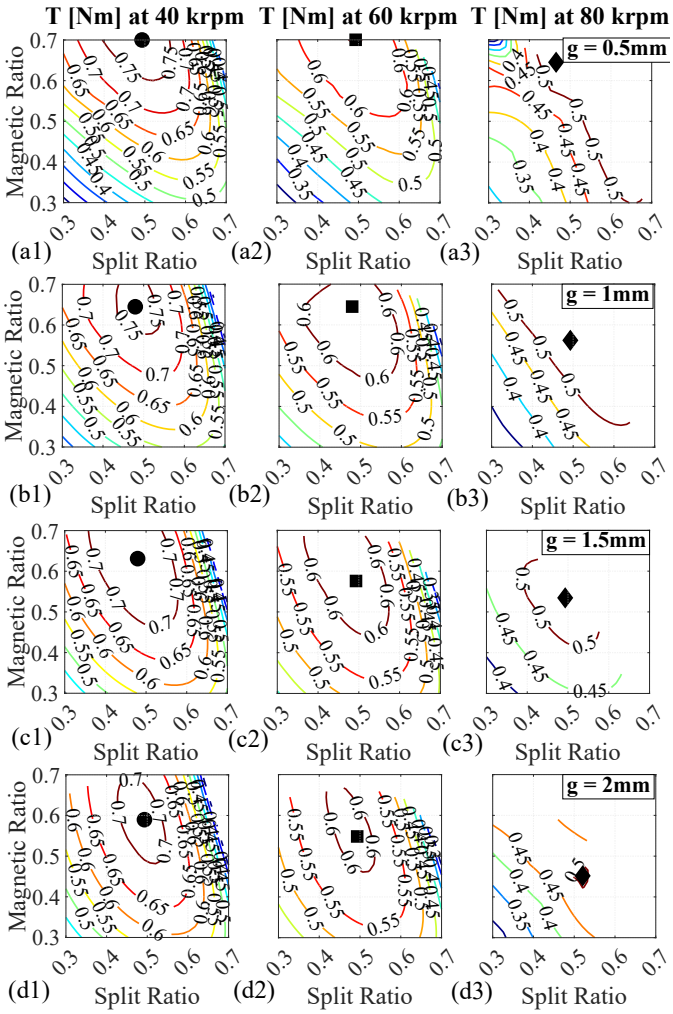

Fig. 10: Torque constant loci contour plot in the $sr - mr$ plane at (1) 40krpm, (2) 60krpm and (3) 80krpm when the airgap thickness is a) 0.5 mm, b) 1 mm, c) 1.5 mm and d) 2 mm

A. Airgap thickness effects

The torque trend with respect to the airgap thickness can be explained analyzing eq. (3) and Fig. 11 which reports the PM flux and the q-axis current at 60 kprm for three different airgap thicknesses. Indeed the torque contour and so the maximum torque location are defined by these two quantities which present different shapes in the $sr-mr$ plane. In particular, the maximum current is located at the bottom-left of the design plane, whereas the PM flux shows an opposite trend. For a given couple of design variables $sr - mr$, the PM flux decreases with the airgap while the current increases. The first behavior can be explained considering that a wider airgap implies higher flux leakages, therefore a lower PM flux linkage for a given first harmonic of the airgap flux density. For the same reason, iron losses decrease when the airgap is higher and, as a consequence, the current increases.

According to the above considerations, for a small airgap the PM flux has a major influence on the maximum torque location, whereas the stator current contribution is more significant when the airgap is increased. As a consequence, the maximum torque is located at high mr when considering low airgap thickness and moves towards lower magnetic ratio for a thicker airgap, as the role of the current contribution becomes more significant. Differently, the optimal sr remains constant for different airgap levels because PM flux linkage and q-axis current have opposite trends when moving horizontally in the design plane.

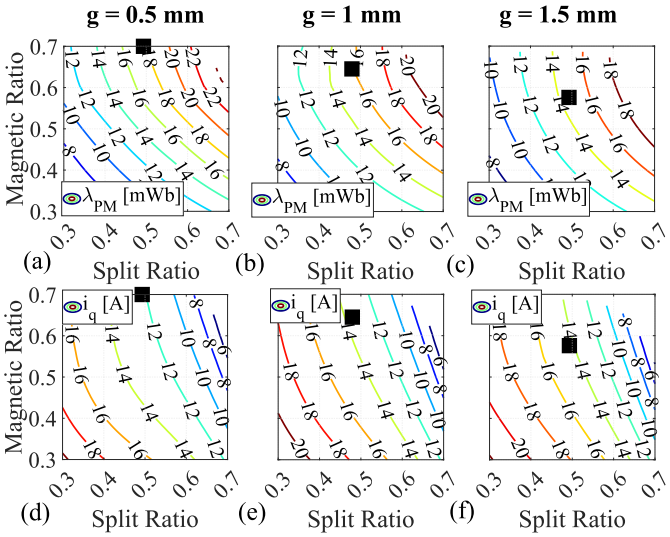

Fig. 11: Contour plot of PM flux (a, b, c) and q-axis current (d, e, f) when the airgap thickness is 0.5 mm (a, d), 1 mm (b, e) and 1.5 mm (c, f) at 60 krpm.

B. Maximum speed effects

The reasons behind the trend of the electromagnetic torque with respect to the speed, for a given airgap thickness, can be inferred by analyzing the contours of the PM flux linkage and the q-axis current shown in Fig. 12 for 40, 60 and 80 krpm.

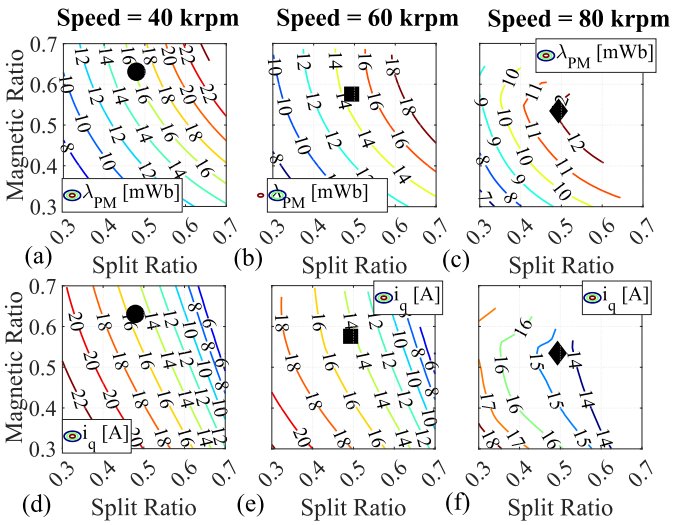

Fig. 12: Contour plot of PM flux (a, b, c) and q-axis current (d, e, f), when the speed is 40 krpm (a, d), 60 kprm (b, e) and 80 krpm (c, f) for an airgap thickness equal to 1.5 mm.

Higher rotational speeds imply a reduction of both PM flux and stator current. The first one decreases due to the higher leakage flux caused by the increment of the magnetic equivalent airgap; the latter due to the higher iron losses, which reduce the allowable maximum current. The maximum torque design features lower magnetic ratio as the speed increases since the rate of decrement (with the speed) of the PM flux is lower than that of the q-axis current. Also in this case, the split ratio of the optimal design remains constant as the speed increases due to the opposite trends of the PM flux and q-axis current when moving horizontally in the design plane.

C. Independent assessment of the high speed limiting factors

In this section the effects of the structural and loss limitations are separately analyzed. In particular, for a given airgap (e.g. 1.5 mm), the design exercise in the $sr - mr$ plane is performed first neglecting the influence of the stator iron losses in the stator current calculation and then neglecting the sleeve increment as the speed increases. Although the superimposition principle is not applicable since the non-linear behavior of the machine does not allow such approximation, this analysis could give some qualitative insights about the trends of the design variables.

Fig. 13 reports the optimal split ratio (a) and magnetic ratio (b) as function of the operating speed when only the structural limitations (solid line), loss ones (dash line) or both of them (dot line) are considered within the design workflow. It is worth to notice that the optimal split ratio tends to decrease when only the structural limitations are considered, while it increases when the design exercise only accounts for the iron losses increment. On the contrary, sleeve or iron losses increments leads to a reduction of the optimal magnetic ratio as the maximum speed increases. The reason behind the decrement of the split ratio when only the structural limitation are considered above 60 krpm can be explained considering the sleeve thickness, whose contours are shown in Fig. 14d,

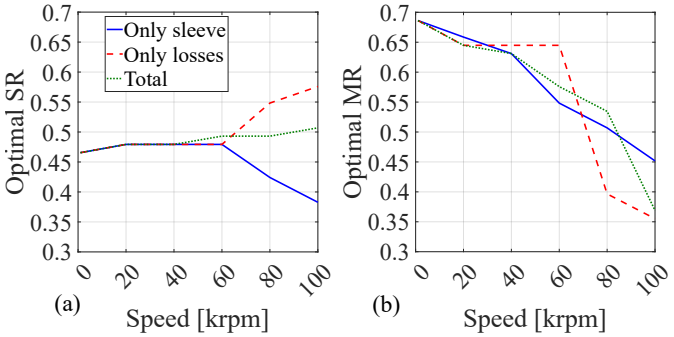

Fig. 13: Optimal split (a) and magnetic (b) ratios as function of the speed.

14e, 14f, and its influence on the PM flux (Fig. 14a, 14b, 14c) when considering different speeds (40 (a,d), 60 (b,e) and 80 (c,f) krpm in Fig. 14). On one hand, a higher split ratio implies a higher rotor radius which in turn leads to an increment of the sleeve thickness. The sleeve thickness increment implies an increment of the PM height h_{PM} to reach the same airgap flux density B_g. On the other hand, lower split ratios result in lower PM flux (since the linear pole pitch is reduced). Until 60 krpm none of these two competitive behaviors is preponderant with respect to the other one and the split ratio basically remains constant. Differently, above 60 krpm, the influence of the sleeve increment plays a major role and therefore the optimal split ratio tends to decrease.

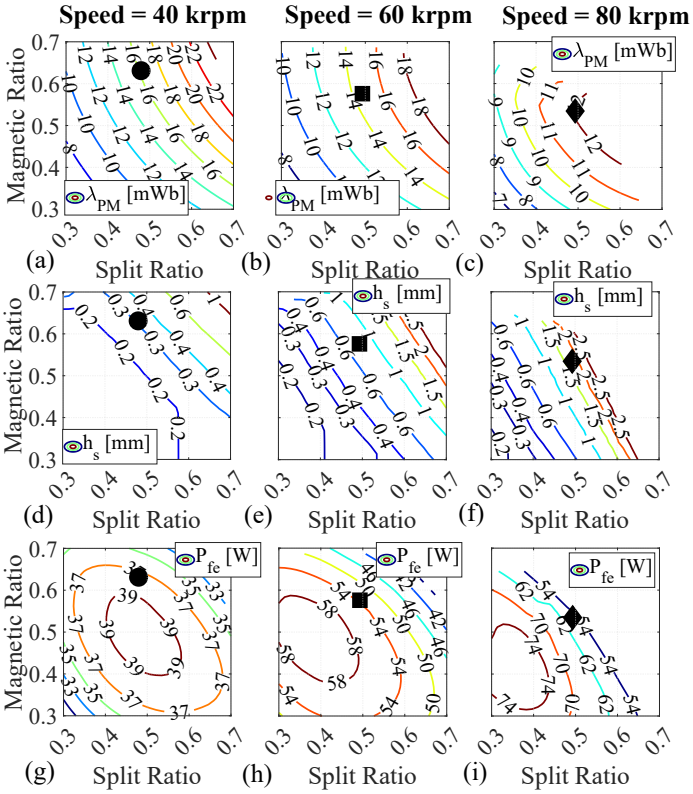

Fig. 14: Costant loci contour plot of PM flux (a, b, c), sleeve thickness (d, e, f) and stator iron losses (g, h, i) when the speed is 40 krpm (a, d, g), 60 kprm (b, e, h) and 80 krpm (c, f, i) and for an airgap thickness equal to 1.5 mm.

Differently, when only the iron losses are considered, the optimal split ratio above 60 krpm increases since in that direction the iron losses tend to decrease as shown in Fig. 14g, 14h and 14i.
The optimal magnetic ratio always tends to decrease whatever the limitation (structural, thermal or both) is considered. The reason behind such decrement has been explained in section IV-B: indeed, the rate of the decrement of the PM flux with the speed is lower than the one of the q-axis current (see Fig. 12).
It can be concluded that the trends of the optimal split and magnetic ratio depend on the concurrent needs of the structural and iron losses effects. In other words, they depend on the sleeve and soft magnetic material affecting the rate of increment of the sleeve and iron losses with the speed.

V. Optimal designs

A. Electromagnetic performance

The trend of the optimal designs in terms of torque and output power as function of the speed are shown in Fig. 15a and 15b. The markers in the same figure represent the FE-evaluated performance, confirming an excellent agreement with the prediction of the proposed method. As previously pointed out, the torque always decreases with the speed due to the increment of iron losses and sleeve thickness and with the airgap thickness. The latter trend is more pronounced at low speed, when the magnetic equivalent airgap almost coincides with the mechanical one. At high speed, the sleeve thickness plays a major role in the definition of the magnetic airgap, therefore the maximum torque designs tend to provide similar performance regardless the airgap thickness.

Regarding the power, the speed increase is beneficial up to 80 krpm for this particular case study whose details are defined in Table I. Beyond this speed the power reaches a plateau or starts to decrease depending on the considered airgap thickness. The improvement of the output power as the maximum speed increases and the airgap decreases comes at the cost of higher rotor losses. Indeed, Fig. 16 shows the sum of the sleeve and PM losses evaluated with FEAs. As expected, the rotor losses increase with the speed and decrease with the airgap. On one hand, the first behavior is due to the higher fundamental frequency of the flux density. On the other hand, the increment of the sleeve thickness drastically increases the magnetic equivalent airgap which in turn determines a reduction of the eddy currents in the rotor components.

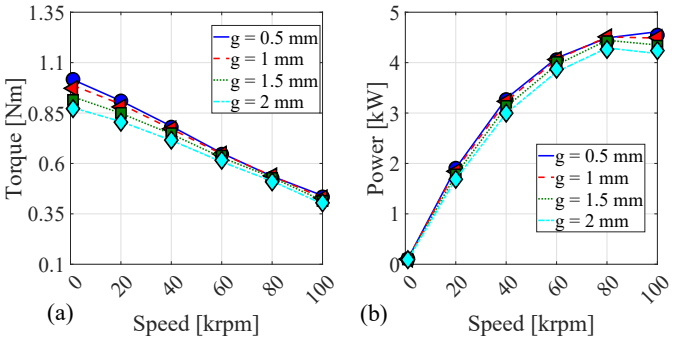

Fig. 15: Torque (a) and power (b) of the optimal designs as function of the speed.

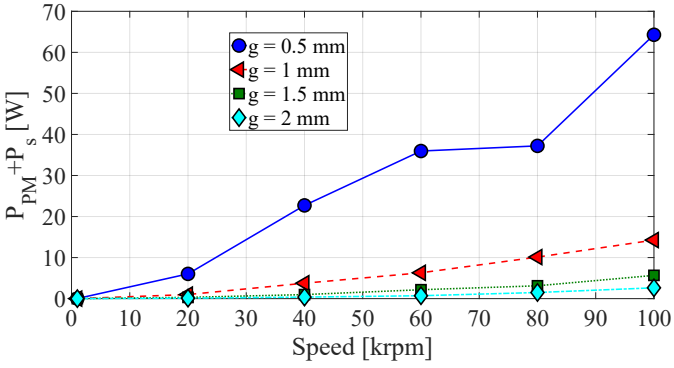

Fig. 16: Rotor losses of the optimal designs as function of the speed.

B. Machine geometries

The trends of the magnetic and split ratio of the maximum torque designs reported in Fig. 10 and justified in the previous section are confirmed by the respective machine cross sections shown in Fig. 17 and whose main parameters are also reported in Table II. The optimal machines share the same rotor radius and feature decreasing tooth and yoke dimensions as the magnetic ratio decreases (with both speed and airgap increment).

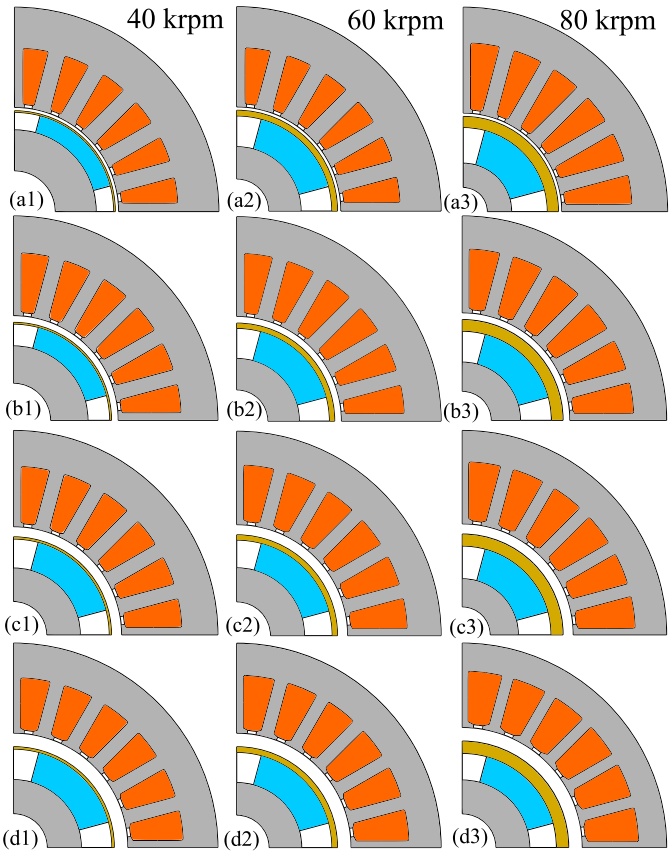

Fig. 17: Cross sections of the optimal machines at (1) 40 krpm, (2) 60 krpm and (3) 80 krpm when the airgap thickness is a) 0.5 mm, b) 1 mm, c) 1.5 mm and d) 2 mm

TABLE II: Optimal machines geometrical parameters (in mm)

Design	Variable	g=0.5mm	g=1mm	g=1.5mm	g=2mm
	w_t	2.44	2.18	2.14	2.05
	l_y	5.96	5.34	5.23	5.02
	h_{PM}	2.58	3.21	4.27	4,50
40krpm	h_s	0.22	0.25	0.31	0.35
	w_t	2.44	2.18	2.00	1.91
	l_y	5.96	5.34	4.91	4.67
	h_{PM}	4.55	4.45	4.09	4.46
60krpm	h_s	0.83	0.76	0.76	0.81
	w_t	2.12	1.96	1.86	1.66
	l_y	5.18	4.79	4.55	4.06
	h_{PM}	5.31	4.56	4.84	3.95
80krpm	h_s	1.63	1.71	1.76	1.81

The trend of PM height with the speed depends on the selected airgap thickness. Indeed, h_{PM} tends to increase with the speed for g up to 1 mm, whereas it remains almost constant when $g = 1.5$ mm and it tends to decrease when $g = 2$mm. The reason of these behaviours can be inferred considering eq. (13) and eq. (14). The magnet dimension h_{PM} is directly proportional to the magnetic voltage drop in the airgap U_g; the latter is in turn proportional to both the equivalent magnetic airgap thickness (mechanical airgap plus sleeve thicknesses) and the airgap flux density B_g. As a consequence, as the speed increases, the magnet thickness is defined by the tradeoff between the decrement of the airgap flux density and the increment of the sleeve thickness. In fact, when the mechanical airgap thickness is small, the sleeve thickness increment has a major effect on U_g, therefore h_{PM} increases. On the contrary, when the mechanical airgap thickness is higher, the sleeve thickness influence on U_g is less pronounced (i.e. even at 100 krpm g is comparable with h_s), thus the reduction of B_g plays a major role and h_{PM} tends to decrease.

C. Thermal performance

The comparative design exercise among different airgap thicknesses and design speeds has been carried out considering the same stator losses. As shown in Fig. 9, the thermal behavior of the machine in the $sr - mr$ plane is approximately the same. This consideration is also valid as the speed increases as shown in Fig. 18a which reports the winding temperatures of the optimal designs. As expected, higher design speed implies a reduction of the Joule losses, therefore the winding temperature tends to decrease with the speed as the iron losses are easier to be dissipated.
It is worth to underline that the rotor losses are not considered within the design process, therefore the temperature of the rotor components need to be verified in a second stage. Fig. 18b, 18c and 18d reports the rotor, sleeve and magnet temperatures of the optimal designs. As expected, the temperatures of those rotor components tend to increase with the speed and decrease with the airgap thickness. Except for the lower airgap thickness (i.e. 0.5 mm), such temperature increment lies within a small range.

D. Selection of the final design

For the considered assumptions listed in Table I, the speed maximizing the power density is either 80 or 100 krpm

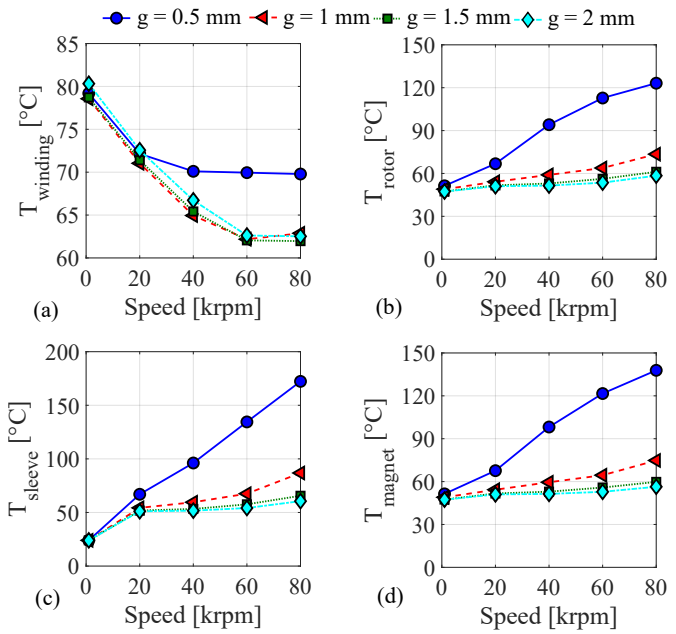

Fig. 18: Winding (a), rotor (b), sleeve (c) and magnet (d) temperatures of the optimal designs at rated conditions.

depending on the airgap thickness. The selection of the latter has been carried out considering the rotor losses. Fig. 19a and 19b show the output power and the rotor losses at 80 and 100 krpm as function of the airgap thickness. It can be seen that the reduction of the airgap thickness (from 2 to 0.5mm) produces a power improvement (circa 7%) as well as a significant increment of the rotor losses (circa 2000%). Although it does not feature the highest power density, the machine with an airgap thickness of 1.5 mm has been selected as final candidate. Indeed, it provides a higher output power with respect to the design reaching 100 krpm guaranteeing also low rotor losses.

The permanent magnet array of the final design has been re-arranged prior the prototyping stage. In particular, a quasi-Halbach configuration featuring the same airgap flux density of the optimal design has been adopted which also allows to decrease the used magnet volume. This change has been done in order to avoid filling inter-polar spaces between the magnets of the standard array to ease the assembly process.

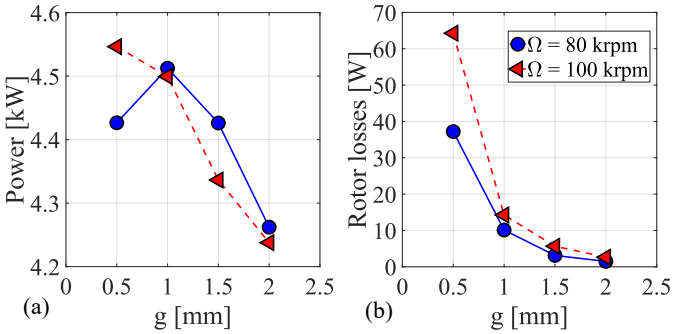

Fig. 19: Power (a) and rotor losses (b) as function of the airgap thickness at 80 and 100 krpm.

VI. Experimental results

The final 4.2kW-80krpm design described in the previous section has been prototyped and tested on an instrumented test rig.

A. Test layout and setup

A view of the main components together with the assembled rotor is reported in Fig. 20.

The manufactured stator and rotor have been encapsulated within a custom designed housing featuring a single spiral water jacket and the inlet and outlet channels for the air-oil mist bearings lubrication, as can be seen in Fig. 21. The latter also reports the complete test rig. It can be seen that the prototype is connected to a load motor via a gearbox (ratio 1:5.975) and a 3.5 Nm torque sensor. An in-house designed SiC three-phase full-bridge converter has been adopted for the machine supply [27], while the control logic has been implemented on a Xilinx Zynq7020 SoC [28].

B. Test results

Several tests have been performed to fully characterize the machine behavior under different operating conditions.

First, the back electromotive force has been measured by a series of no-load tests. Fig. 22a shows the phase to phase

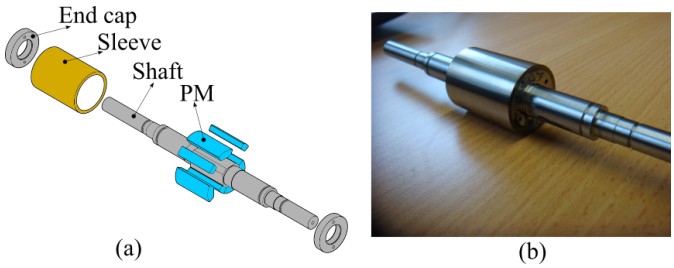

Fig. 20: (a) Rotor assembly process; b) assembled rotor.

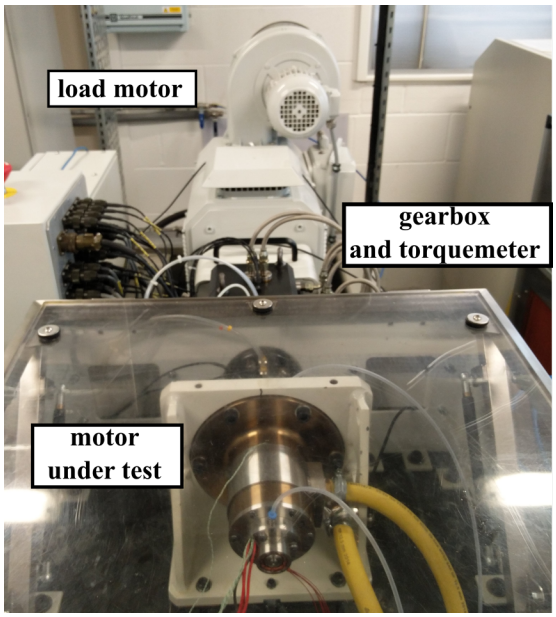

Fig. 21: Experimental setup layout.

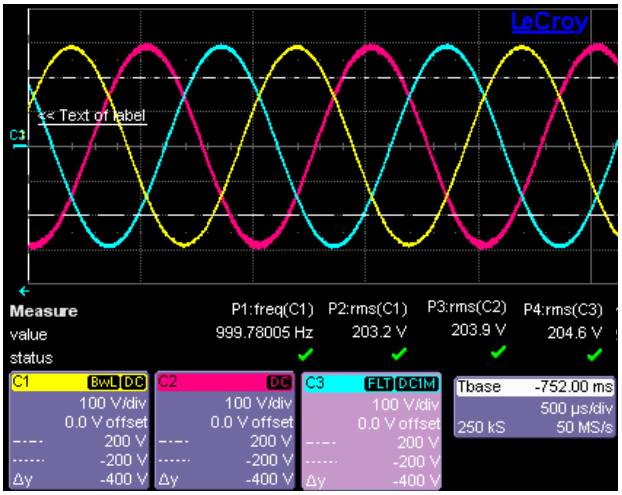

(a)

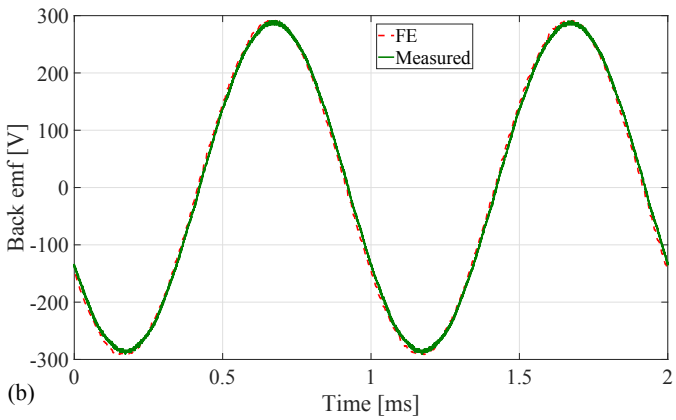

(b)

Fig. 22: back emf test at 30 krpm: (a) scope capture showing the the phase-to-phase voltages during the no-load test; (b) comparison between measured and FE phase-to-phase no-load voltages.

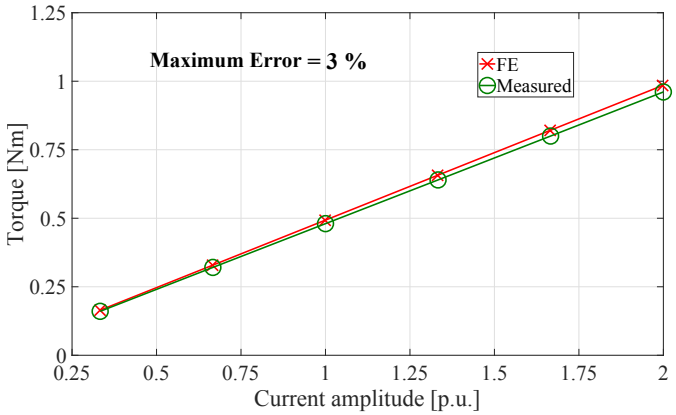

Fig. 23: Comparison between FE computed and measured torque at MTPA condition.

voltage measured at 30 krpm, whereas the excellent agreement between the FE-computed and measured profiles is reported in Fig. 22b.

Fig. 23 reports the measured torque compared to the FE-one for several current amplitudes (up to 2 times the rated one). A good agreement can be observed. The maximum error is about 3% and it can be mainly ascribed to the impact of the manufacturing tolerances as well as the different magnetic behaviour of the constituent materials which can play

a significant role in the performance of small-size machines.

Fig. 24a shows the comparison between the FE-computed and measured internal power factor at MTPA condition, while the efficiency map in the speed-current plane is reported in Fig. 24b. Both power factor and efficiency have been measured using a power analyzer. It is worth to notice that both power factor and efficiency are in good agreement with FE estimations. Indeed, the maximum error is about 1.4% for the power factor, while the average efficiency error is 1.5% (the maximum error is about 15%); these mismatches can be ascribed to several factors including the manufacturing tolerances and the behavior of the magnetic materials [29].

Fig. 25a reports an acceleration test at no-load up to 38 krpm, while Fig. 25b shows the d- and q-axis voltages during the same test. Above 38 kprm, the measured vibrations exceeded the safety limits, therefore tests at higher speed have not been performed; by analysing the vibration spectrum, a non-perfect alignment of the bearings within the housing has been identified as the most probable cause of such vibrations, which are neither related to the final design nor to the test rig.

Finally, the thermal behavior of the machine at rated conditions and for different operating speed is shown in Table III, where the measured winding maximum temperature is compared to the one estimated using a commercial solver [26]. A good match can be observed for all the considered operating points.

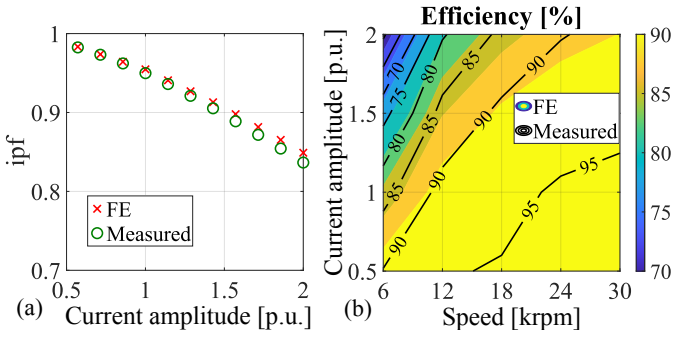

Fig. 24: Comparison between (a) FE computed and measured power factor at MTPA condition and (b) FE computed and measured efficiency in the speed-current plane.

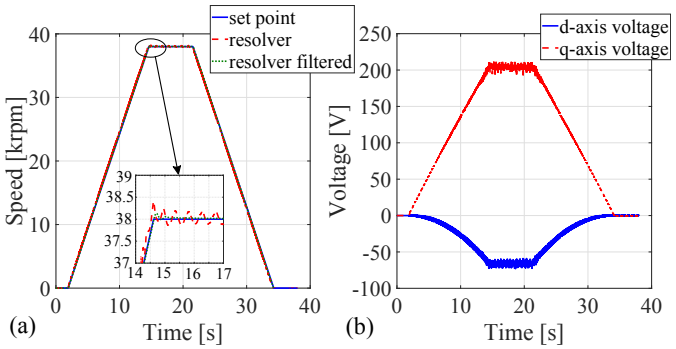

Fig. 25: Speed test: (a) reference speed against the measured and measured-filtered ones; b) d- and q-axis voltages.

TABLE III: Comparison between measured and FE temperatures.

	Temperatures [deg.]				
	6krpm	12krpm	18krpm	24krpm	30krpm
FE	55	56	56	57	58
EXP	47	50	52	52	56

VII. Conclusion

This paper has proposed a comprehensive and accurate design methodology for high-speed surface-mounted permanent magnets synchronous machines. The proposed design procedure, which reduces the independent variables to two and uses only few FE simulations to correct the analytical modelling errors, has been used to systematically asses the maximum power capability as function of the maximum speed and the airgap thickness.

It has been shown that the rise of the iron losses and sleeve thickness limits the maximum power that can be achieved increasing the speed. Indeed, there is a speed value above which the power density does not further increase. This threshold speed is slightly reduced when considering a thicker airgap thickness. The increment of the latter also leads to a torque decrement since a wider airgap implies higher flux leakage.

As the speed or the airgap thickness increase, the maximum torque design moves towards lower magnetic ratios, since in that direction there is the optimal compromise between the competitive needs of maximizing the PM flux linkage and the q-axis current which are the variables affecting the torque behaviour. On the contrary, the optimal split ratio is neither affected by the speed nor by the airgap thickness; indeed, it remains almost constant. Such behaviour is determined by the competitive needs of the sleeve increment (which would lead to a lower rotor radius) and the iron losses increment (which would lead to a higher rotor radius). In conclusion, the change with the speed of the machine geometry featuring the highest torque depends on the materials selected for laminations and sleeve, which define the rate of change of iron loss and sleeve thickness.

In order to validate the design considerations, an 4.2kW-80kprm surface permanent magnet synchronous machine has been prototyped and tested. The reasons behind the selection of the final design have been discussed including the influence of the rotor eddy current losses. Several experimental tests have been reported including no-load voltage profile at a fixed speed, average torque as function of current amplitude, power factor and efficiency. The comparison of such quantities with the respective predicted values shows an acceptable agreement endorsing both design methodology and general considerations.

References

[1] J. Cekani, F. G. Capponi, G. De Donato, and F. Caricchi. Mechanical flux weakening methods for the achievement of a very wide constant power speed range in automotive applications. *IEEE Journal of Emerging and Selected Topics in Power Electronics*, 10(3):3443–3458, 2022.

[2] L. Wang, Z.Q. Zhu, H. Bin, and L. M. Gong. Recent developments of high speed electrical machine drive systems. In *2021 Sixteenth International Conference on Ecological Vehicles and Renewable Energies (EVER)*, pages 1–10, 2021.
[3] J. Ou, Y. Liu, and M. Doppelbauer. Comparison study of a surface-mounted pm rotor and an interior pm rotor made from amorphous metal of high-speed motors. *IEEE Transactions on Industrial Electronics*, 68(10):9148–9159, 2021.
[4] M.-S. Lim, J.-M. Kim, Y.-S. Hwang, and J.-P. Hong. Design of an ultra-high-speed permanent-magnet motor for an electric turbocharger considering speed response characteristics. *IEEE/ASME Transactions on Mechatronics*, 22(2):774–784, 2017.
[5] M. Johnson, K. Hanson, and E. L. Severson. Normalized analytical model of stresses in a surface mounted permanent magnet rotor. In *2021 IEEE Energy Conversion Congress and Exposition (ECCE)*, pages 3928–3935, 2021.
[6] N. Bianchi, S. Bolognani, and F. Luise. Potentials and limits of high-speed pm motors. *IEEE Transactions on Industry Applications*, 40(6):1570–1578, 2004.
[7] N. Bianchi, S. Bolognani, and F. Luise. Analysis and design of a pm brushless motor for high-speed operations. *IEEE Transactions on Energy Conversion*, 20(3):629–637, 2005.
[8] A. Tenconi, S. Vaschetto, and A. Vigliani. Electrical machines for high-speed applications: Design considerations and tradeoffs. *IEEE Transactions on Industrial Electronics*, 61(6):3022–3029, 2014.
[9] T.-W. Lee and D.-K. Hong. Rotor design, analysis and experimental validation of a high-speed permanent magnet synchronous motor for electric turbocharger. *IEEE Access*, 10:21955–21969, 2022.
[10] F. Zhang, G. Du, T. Wang, G. Liu, and W. Cao. Rotor retaining sleeve design for a 1.12-mw high-speed pm machine. *IEEE Transactions on Industry Applications*, 51(5):3675–3685, 2015.
[11] G. Gallicchio, M. Di Nardo, M. Palmieri, A. Marfoli, M. Degano, C. Gerada, and F. Cupertino. High speed synchronous reluctance machines: Modeling, design and limits. *IEEE Transactions on Energy Conversion*, 37(1):585–597, 2022.
[12] D.C. Hanselman. *Brushless Permanent Magnet Motor Design*. Magna Physics Publishing, 2006.
[13] T. Jokinen, V. Hrabovcova, and J. Pyrhonen. *Design of rotating electrical machines*. John Wiley & Sons, 2013.
[14] D.-H. Jung, J.-K. Lee, J.-Y. Kim, I. S. Jang, J. Lee, and H.-J. Lee. Design method of an ultrahigh speed pm motor/generator for electric-turbo compounding system. *IEEE Transactions on Applied Superconductivity*, 28(3):1–4, 2018.
[15] Y. Wang, Z.-Q. Zhu, J. Feng, S. Guo, Y. Li, and Y. Wang. Rotor stress analysis of high-speed permanent magnet machines with segmented magnets retained by carbon-fibre sleeve. *IEEE Transactions on Energy Conversion*, 36(2):971–983, 2021.
[16] H. Fang, D. Li, R. Qu, J. Li, C. Wang, and B. Song. Rotor design and eddy-current loss suppression for high-speed machines with a solid-pm rotor. *IEEE Transactions on Industry Applications*, 55(1):448–457, 2019.
[17] A. Binder, T. Schneider, and M. Klohr. Fixation of buried and surface-mounted magnets in high-speed permanent-magnet synchronous machines. *IEEE Transactions on Industry Applications*, 42(4):1031–1037, 2006.
[18] J.-H. Ahn, J.-Y. Choi, C. H. Park, C. Han, C.-W. Kim, and T.-G. Yoon. Correlation between rotor vibration and mechanical stress in ultra-high-speed permanent magnet synchronous motors. *IEEE Transactions on Magnetics*, 53(11):1–6, 2017.
[19] H. A. Khan, F. Khan, S. Khan, N. Ahmad, J. B. Soomro, and I. Sami. Design and performance investigation of 3-slot/2-pole high speed permanent magnet machine. *IEEE Access*, 9:41603–41614, 2021.
[20] G. Du, N. Huang, H. He, G. Lei, and J. Zhu. Parameter design for a high-speed permanent magnet machine under multiphysics constraints. *IEEE Transactions on Energy Conversion*, 35(4):2025–2035, 2020.
[21] S. Ferrari and G. Pellegrino. Feafix: Fea refinement of design equations for synchronous reluctance machines. *IEEE Transactions on Industry Applications*, 56(1):256–266, 2020.
[22] M. Di Nardo, G. Gallicchio, M. Palmieri, A. Marfoli, G. Lo Calzo, M. Degano, C. Gerada, and F. Cupertino. High-speed synchronous reluctance machines: Materials selection and performance boundaries. *IEEE Transactions on Transportation Electrification*, 8(1):1228–1241, 2022.
[23] Thomas A Lipo. *Introduction to AC machine design*. John Wiley & Sons, 2017.
[24] J. N. Reddy. *Mechanics of laminated composite plates and shells: theory and analysis*. CRC press, 2003.
[25] Wilhelm Flügge. *Stresses in shells*. Springer Science & Business Media, 2013.
[26] "Motor-CAD". Accessed: Jan. 11, 2021. [Online]. Available: https://www.motor-design.com.
[27] Giovanni Lo Calzo, Pericle Zanchetta, Chris Gerada, Alberto Gaeta, and Fabio Crescimbini. Converter topologies comparison for more electric aircrafts high speed starter/generator application. In *2015 IEEE Energy Conversion Congress and Exposition (ECCE)*, pages 3659–3666, 2015.
[28] A. Galassini, G. Lo Calzo, A. Formentini, C. Gerada, P. Zanchetta, and A. Costabeber. ucube: Control platform for power electronics. In *2017 IEEE Workshop on Electrical Machines Design, Control and Diagnosis (WEMDCD)*, pages 216–221, 2017.
[29] Andrea Credo, Ilya Petrov, Juha Pyrhönen, and Marco Villani. Impact of manufacturing stresses on multiple-rib synchronous reluctance motor performance. *IEEE Transactions on Industry Applications*, pages 1–10, 2022.

Gianvito Gallicchio received the B.Sc. (Hons.) and M.Sc. (Hons.) degrees in electrical engineering from the Politecnico di Bari, Bari, Italy, in 2016 and 2018, respectively. He is currently working toward the Ph.D. degree with the Electrical Machines and Drives Group, Politecnico di Bari, Bari, Italy. His main research interests include the design, modeling and analysis of permanent magnet and synchronous reluctance machines for both traction and high-speed applications, as well as the analysis, modeling and optimization of magnetic couplings.

Mauro Di Nardo (M'18) received the M.Sc. (Hons.) degree in electrical engineering from the Polytechnic University of Bari, Italy, in 2012, and the Ph.D. degree in electrical machine design from the University of Nottingham, U.K., in 2017. From 2017 to 2019, he was the technical lead of the AROL R&D team within the Polytechnic University of Bari working on electrical drives design for mechatronics applications. Since the 2019, he is with the Power Electronics and Machine Control Group of the University of Nottingham as Research Fellow working on wide variety of projects. His research interests include the analysis, modelling, and design optimizations of permanent magnet and synchronous reluctance machines for automotive, aerospace and household sectors, induction motor for industrial applications as well as niche machine topologies such as bearingless and hysteresis motor. He has been serving as an Associate Editor for the Open Journal of Industry Applications since 2021.

Marco Palmieri received the M.Sc. and Ph.D. degrees in electrical engineering from Politecnico di Bari, Italy, in 2011 and 2016, respectively. From 2017 to 2022 he was a postdoctoral researcher at the Politecnico di Bari, where he joined the electrical machines and drives research group. Since 2022, he is Assistant Professor at the Università degli studi della Basilicata. In 2014 he joined the Power Electronics, Control, and Machines Research Group of the University of Nottingham, working on electrical machines for aeronautical applications. In 2019 he was visiting researcher with the Laboratory of Actuation Technology of the Saarland University, working on sensorless control of Permanent Magnet Machines. His research interests include modelling and analysis of electrical machines as well as the design of high-speed electrical machines by means of optimization algorithms and finite element analysis. Dr. Palmieri co-received the Prize Paper Award from the IEEE Industrial Electronics Society Electrical Machines Committee in 2015.

Mohammad Reza Ilkhani received MS.C and PhD in mechanical engineering with a focus on experimental modal analysis and rotordynamic from the Iran University of Science and Technology (IUST) in 2012 and 2017. Following multiple years of industrial experience in the gas turbine and power generation industries, he moved to the University of Nottingham in 2019 as a Research Fellow. He is currently a Senior Researcher within the Power Electronic Machine and Control group at the same institution working on a wide variety of research topics ranging from the mechanical design, rotordynamic and noise vibration and harshness analysis of rotating machinery's for propulsion applications.

Michele Degano (SM'21) received his Master's degree in Electrical Engineering from the University of Trieste, Italy, in 2011, and his Ph.D. degree in Industrial Engineering from the University of Padova, Italy, in 2015. Between 2014 and 2016, he was a postdoctoral researcher at The University of Nottingham, UK, where he joined the Power Electronics, Machines and Control (PEMC) Research Group. In 2016 he was appointed Assistant Professor in Advanced Electrical Machines, at The University of Nottingham, UK. He was promoted Associate Professor in 2020. His main research focuses on electrical machines and drives for industrial, automotive, railway and aerospace applications, ranging from small to large power. He is currently the PEMC Director of Industrial Liaison leading research projects for the development of hybrid electric aerospace platforms and electric transports.

Chris Gerada (SM'12) is an Associate Pro-Vice-Chancellor for Industrial Strategy and Impact and Professor of Electrical Machines. His principal research interest lies in electromagnetic energy conversion in electrical machines and drives, focusing mainly on transport electrification. He has secured over £20M of funding through major industrial, European and UK grants and authored more than 350 referred publications. He received the Ph.D. degree in numerical modelling of electrical machines from The University of Nottingham, Nottingham, U.K., in 2005. He subsequently worked as a Researcher with The University of Nottingham on high-performance electrical drives and on the design and modelling of electromagnetic actuators for aerospace applications. In 2008, he was appointed as a Lecturer in electrical machines; in 2011, as an Associate Professor; and in 2013, as a Professor at The University of Nottingham. He was awarded a Research Chair from the Royal Academy of Engineering in 2013. Prof. Gerada served as an Associate Editor for the IEEE Transactions on Industry Applications and is the past Chair of the IEEE IES Electrical Machines Committee.

Francesco Cupertino (M'08–SM'12) received the Laurea and Ph.D. degrees in electrical engineering from the Politecnico di Bari, Bari, Italy, in 1997 and 2001, respectively. Since 2001, he has been with the Department of Electrical and Information Engineering, Politecnico di Bari, Bari, Italy, where he is currently a Full Professor of converters, electrical machines, and drives. He is the Scientific Director of four public/private laboratories at Politecnico di Bari that enroll more than 50 researchers; the laboratory Energy Factory Bari, with GE AVIO, aimed at developing research projects in the fields of aerospace and energy; the More Electric Transportation laboratory, with CVIT SpA (BOSCH Group), aimed at developing technologies for sustainable mobility; Cyber Physical Systems AROL Bari, with AROL SpA, focused on closure systems for food and beverage; Innovation for Mills, with Casillo Group and Idea75, focused in the Industry4.0 applications for wheat processing. He has authored or coauthored more than 130 scientific papers on these topics. His research interests include the design of synchronous electrical machines, motion control of high performances electrical machines, applications of computational intelligence to control, and sensorless control of ac electric drives. Dr. Cupertino was the recipient of two Best Paper Awards from the Electrical Machines Committee of the IEEE Industry Application Society and from the homonymous Committee of the IEEE Industrial Electronics Society, in 2015. He is currently the rector of Politecnico di Bari.